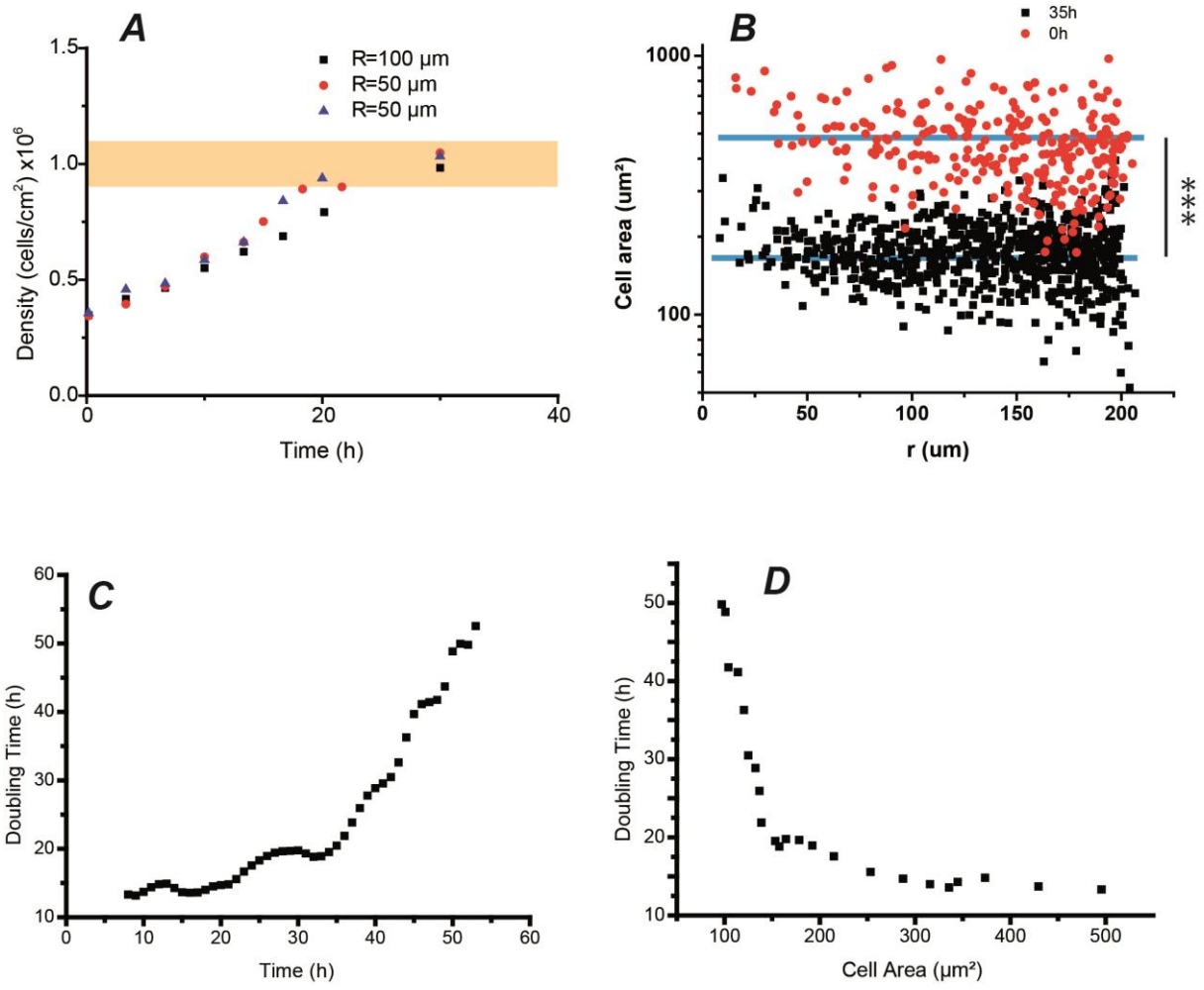

Supplementary Figure 1: Proliferation within the monolayer. A) Cell density in the patches increased in the first 30 h before stabilizing at ~10^6cells/cm^2. The origin of the times is the confluence. The orange line represents the density at which the monolayer stabilizes (± SD) (n=44 patches of various diameters over 4 experiments) – histones H2B-mCherry clones). **B)** Cell size distribution in a patch (R=200µm) immediately after confluence and after 35h. There is no dependency of the cell size with respect to its position in the domain. Horizontal blue lines denote the mean values (***: $p < 0.005$, 2-sample t test, n = 1000). **C)** and **D)** The doubling time of the monolayer population increases with time and with cell density. Small cell sizes correspond to long times. Note that this doubling time corresponds to the number of cells adhering to the surface. The cells extruded from the monolayer are excluded from this measurement. (Representative curves, 15 replicates over 3 independent experiments).

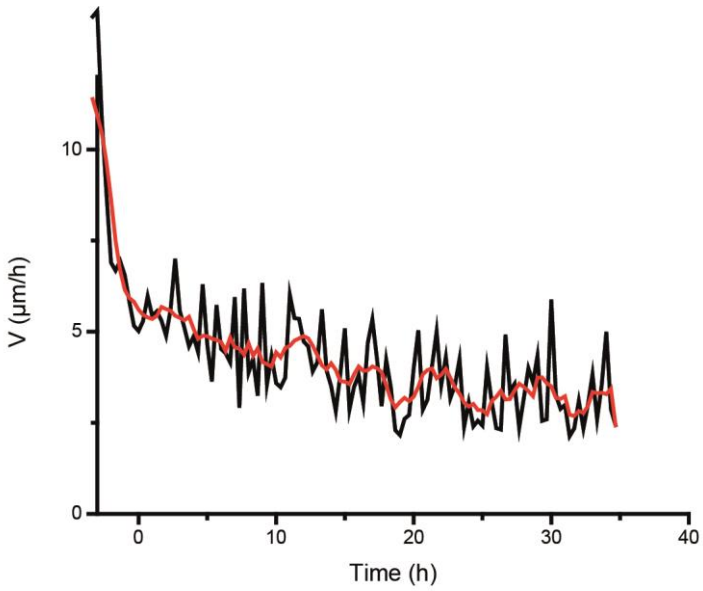

Supplementary Figure 2: Contact inhibition of locomotion in a large monolayer. The monolayer was cultured over an entire Petri dish and analyzed within a R=100 µm region to allow for a direct comparison with confined monolayers. No oscillation was observed. Representative plot, 10 replicates for analysis disks of radii ranging from 50 to 200 µm.

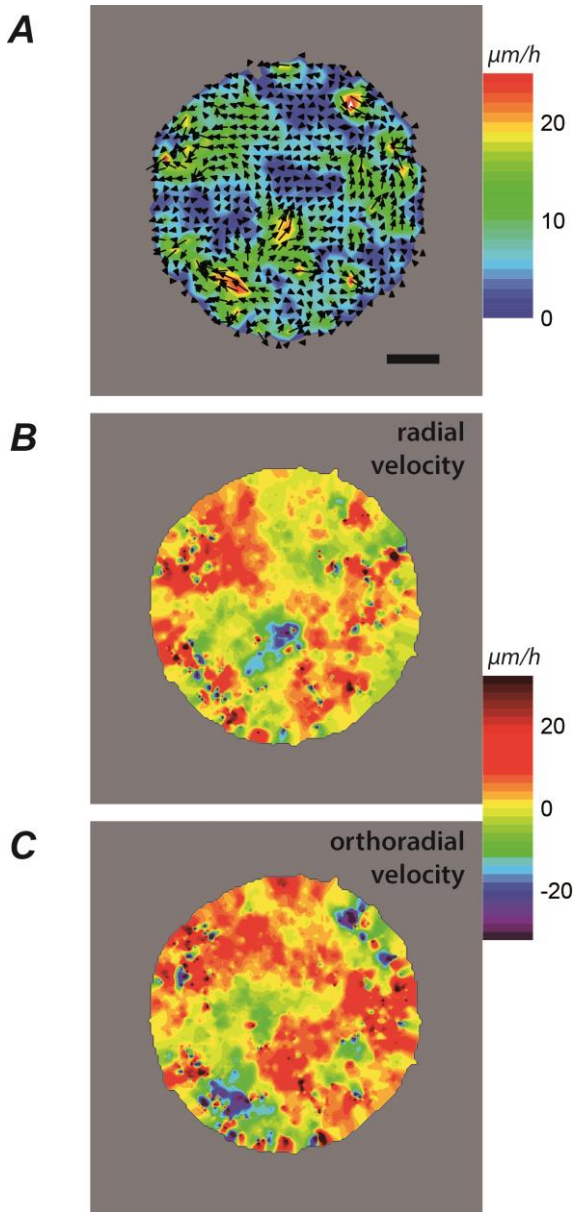

Supplementary Figure 3: Velocity fields are highly heterogeneous. A) Velocity field with in the patch. Arrows give the directionality and the color code is the amplitude. **B)** and **C)** are respectively the radial and orthoradial components of the velocity field depicted in A). Since relatively high cell densities are attained, phase contrast images present a halo at the border that makes velocity measurement by PIV difficult. Consequently, the outermost values (typically within one window size) are underestimated. Bar= 40 μm.

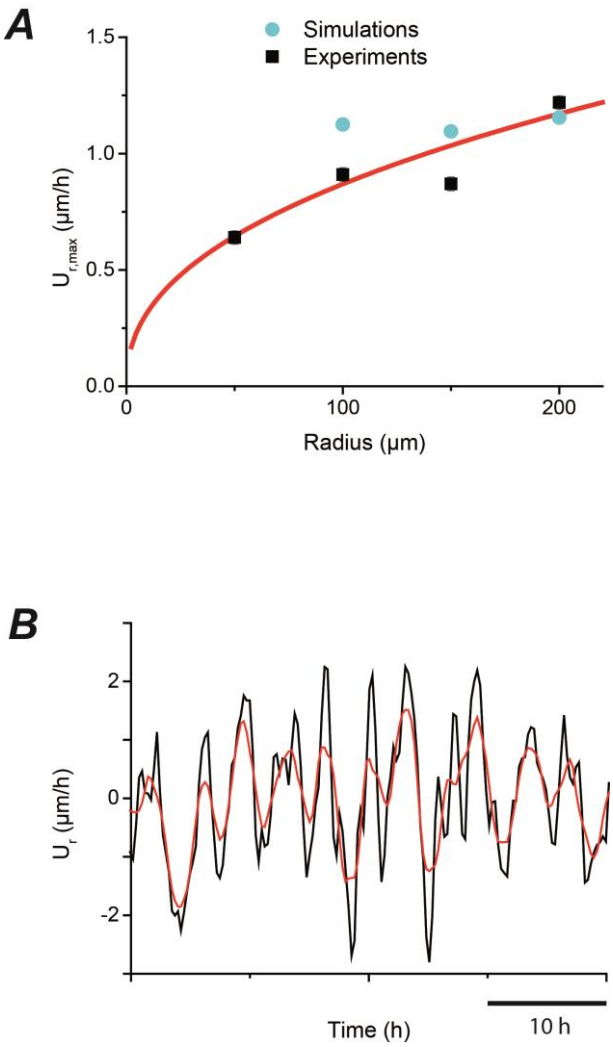

Supplementary Figure 4: The maximum of the radial speed increases with the patch radius. A) The radial component of the velocity is maximal at mid-point between the patch center and its boundary (Fig. 2D). The maximal value increases with the patch dimension. The red line is a fit with a power law $U_{r,max} \propto R^{\alpha}$, yielding $\alpha = 0.4 \pm 0.1$. Data was averaged over 30 hours after confluence. Error bars are SDs. The blue points result from simulations based on our model with conditions identical to the experiments. Between 2 and 13 curves were analyzed for each size over 4 experiments. **B)** Simulated dynamics of the breathing oscillations of $U_r(t)$. Comparing with Fig. 2E, the density was kept constant in the simulations and therefore the damping of the oscillations due to cell jamming at high densities is not observed.

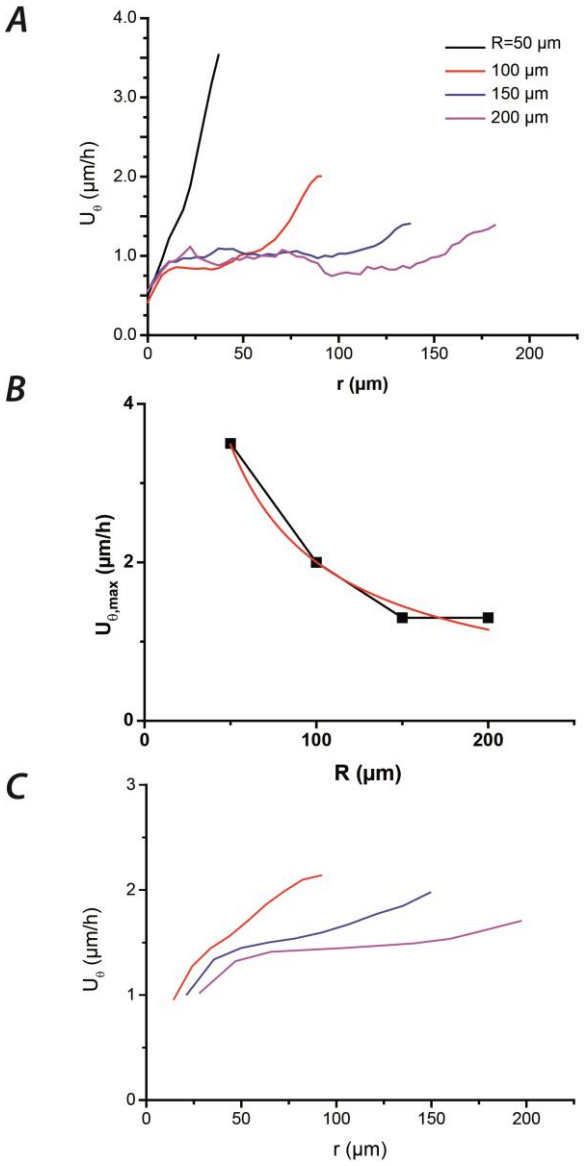

Supplementary Figure 5: Orthoradial velocity. A) The orthoradial component of the velocity is maximal at the patch boundary. n= 2-13 curves for each size, 4 experiments. **B)** Although this orthoradial component cannot be rescaled as does the radial component, its maximal value decrease with the patch radius. The red line is a fit with a power law $U_{\theta max} \propto R^{\alpha}$, yielding α = -0.8±0.1. Data was averaged over 30 hours after confluence. Error bars are SDs. n= 15. **C)** Simulated profile of the orthoradial component of the velocity performed in identical conditions as A).

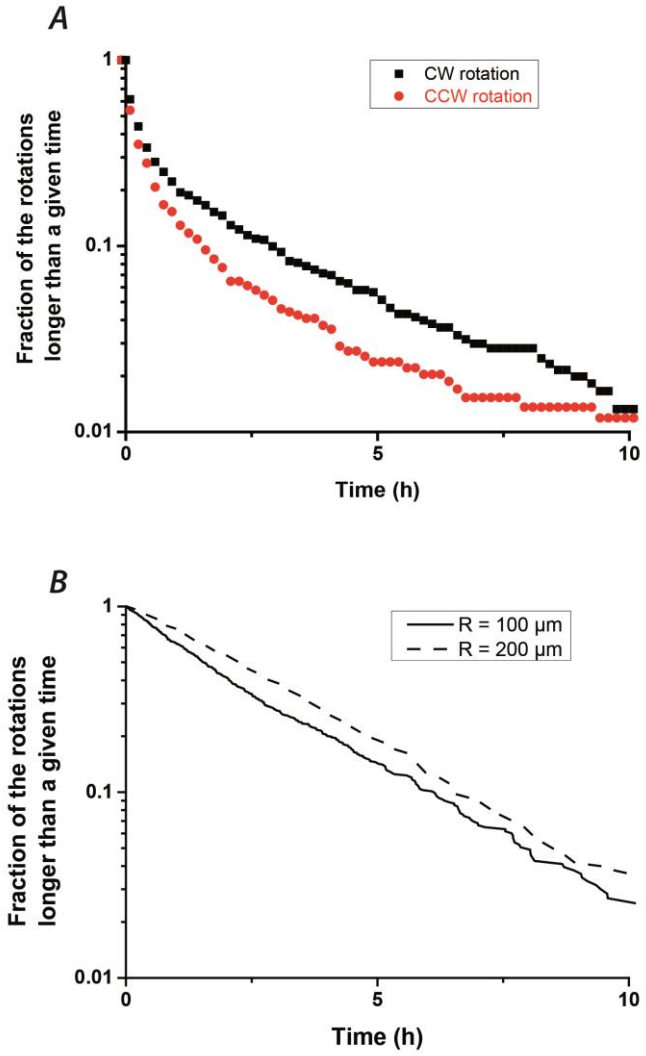

Supplementary Figure 6: The clockwise global rotation is favored over the counter clockwise rotation. A) The times of rotation were compiled and concatenated on 49 patches of radii ranging from 50 to 200 µm (no dependence with the domain radius was observed). The two distributions are significantly different (n ~ 600 rotations in each direction. p = 0.019 – Kolmogorov-Smirnov test). **B)** Simulations based on the model showed stochastic changes of direction (exponential distribution). The analysis was the same as in A). Quantitatively, the rotation durations were comparable for theory and experiments but the experiments showed more short rotations. The Left-Right asymmetry evidenced in the experiments was obviously not present in the simulations since particles were assumed to be achiral.

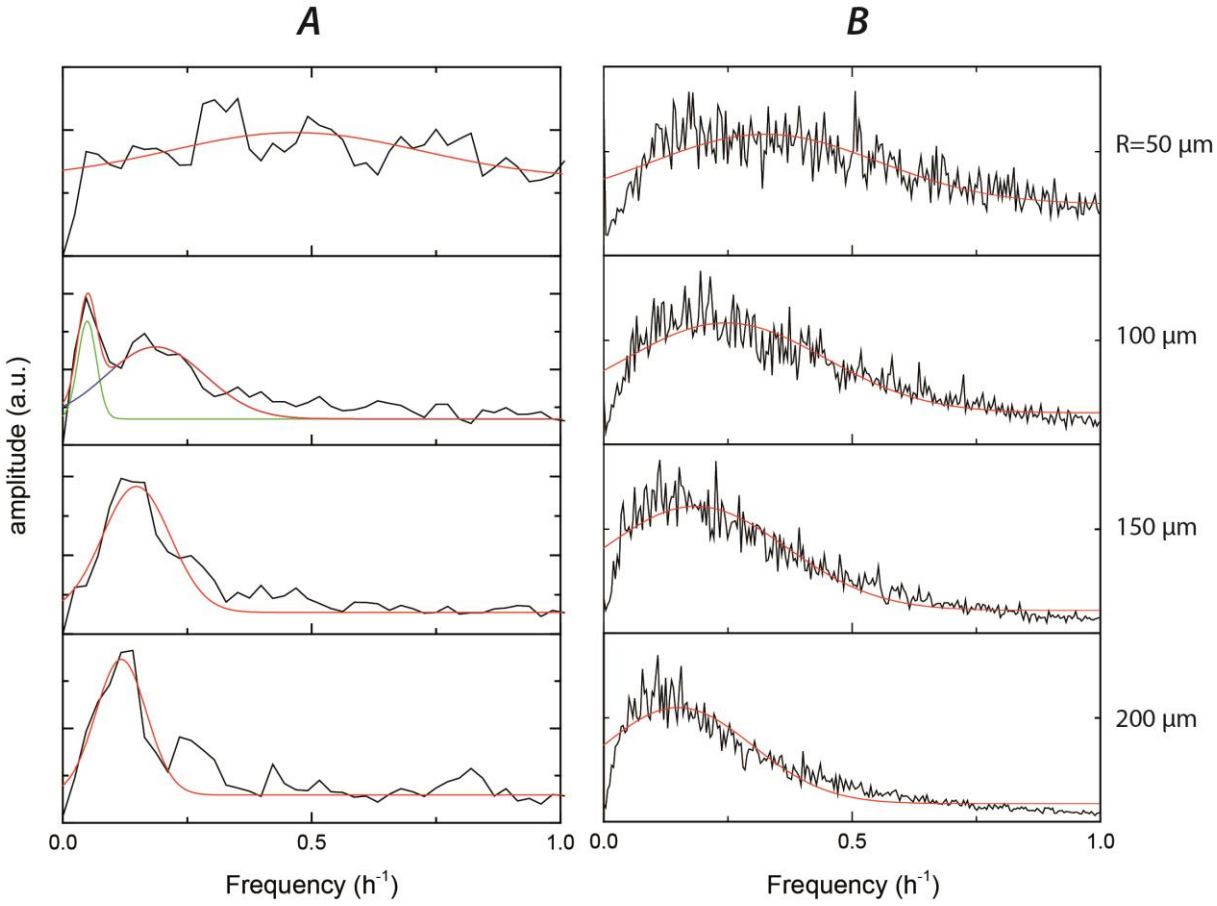

Supplementary Figure 7: The oscillations of the radial velocity define a breathing period. A) Black lines are the FFTs of the oscillations pattern of U_r. Recordings similar to the one represented in Fig. 2E were analyzed after subtraction of their mean value. 5 to 21 fluctuation spectra from 4 experiments were analyzed for each size. Red lines are fits by Gaussian functions that were used to measure the peak position. For R=100 µm, a second peak at very low frequency was observed but was not taken into account in the analysis. **B)** A similar approach was taken on the radial velocity profiles generated by the simulations based on the model. Here, too, a well-defined breathing frequency was obtained**.** n=8, t=256h each.

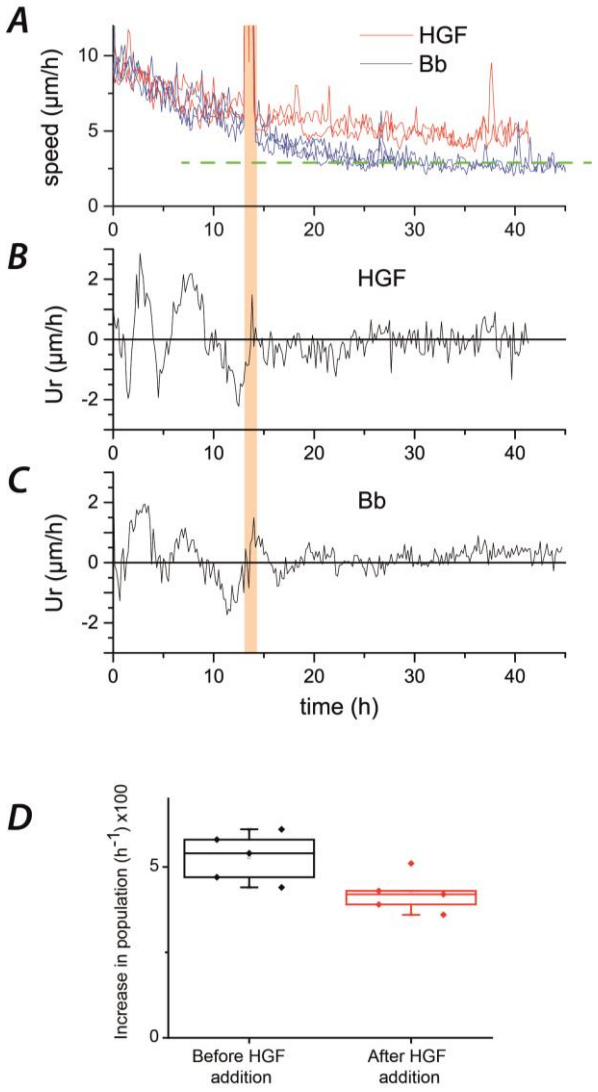

Supplementary Figure 8: Oscillations result from the collective motion and involve contractility. The orange vertical bar corresponds to the introduction of the drug. R = 175µm. **A)** Blebbistatin (Bb) did not affect the cell average speed whereas cells treated with HGF remained faster than the control (dashed green line). **B)** HGF suppressed the oscillations demonstrating the role of collective motion and coordination in their generation (Representative plot, 5 replicates). **C)** Bb also suppressed the oscillations demonstrating the importance of contractility although cells were still motile (Representative plot, 5 replicates). **D**) HGF addition did not result in an increase in population ($p=0.016$, two sample t test, $n=5$ over 5 experiments). HGF was added 13h after confluence and proliferation was monitored until 25 h after confluence. See also Supplementary Figure 9.

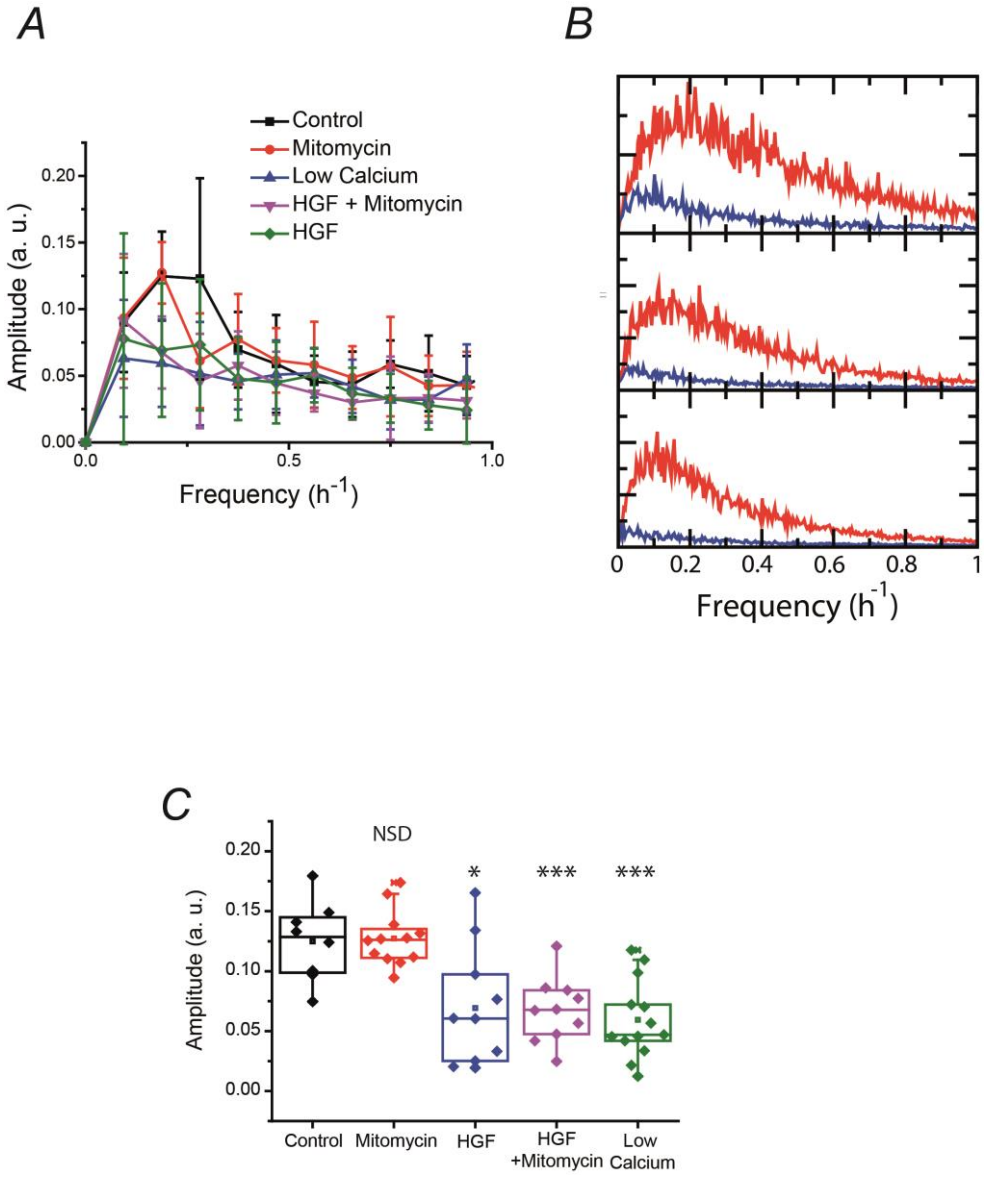

Supplementary Figure 9: The breathing radial oscillations are a collective, proliferation-independent phenomenon. A. Frequency spectra obtained in different conditions. A peak is visible in the control and mitomycin conditions, demonstrating that the oscillations are independent from proliferation. There is no detectable peak in presence of HGF or in low-Calcium buffer showing that it emerges from a collective effect. R= 100 µm. Each curve results from averaging 8 to 14 individual spectra over 2 experiments, error bars are SDs. **B.** Cell velocity alignment promotes breathing oscillations in simulations: Spectra of mean radial velocity in simulations with velocity alignment (red, same data as in Supp. Fig. 4) and without velocity alignment for the same parameter otherwise (see Supplementary Methods 1). The simulation radii are 100 µm, 150 µm, 200 µm from top to bottom. **C.** Quantification of the amplitude of the 0.1875 h^{-1} peak in the Fourier Transform. (*:p<0.05; ***: p<0.005, 2-sample t-test, n= 50, 2 experiments).

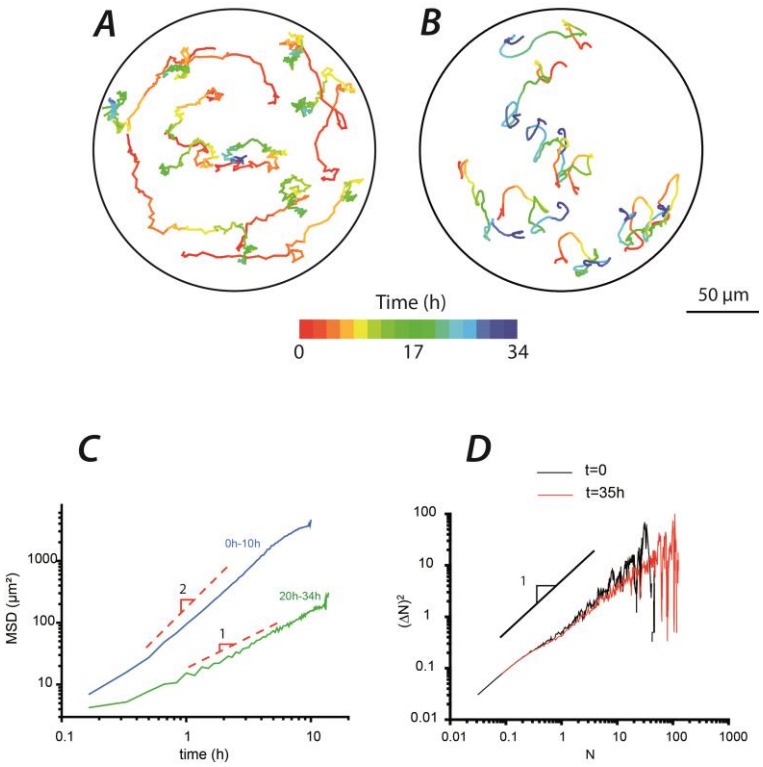

Supplementary Figure 10: Cells are not in a jammed state. A) Trajectories of 10 cells in a 200µm radius domain. Positions are color-coded. Initially, most of the displacements result from the global rotation of the cells. **B)** Simulated trajectories. Since the density was kept constant in the simulations, we do not observe the very large stretching of the trajectories immediately after confluence. Importantly, in the experiments and in the simulations cells move appreciably up to ~ 30 h. in this regime, they are still far from the high density jammed state. **C)** The MSDs obtained by tracking 10 cells show that the cell behavior remains ballistic for times smaller than 10h. (n=4 domains). When time is larger than 20h, the cells have a diffusive-like behavior (effective diffusion coefficient ~ 3.2 ± 0.2 µm²/h). **D)** The fluctuations ΔN are proportional to $\sqrt{N}$ meaning that the system does not exhibit anomalous density fluctuations up to 35 h.

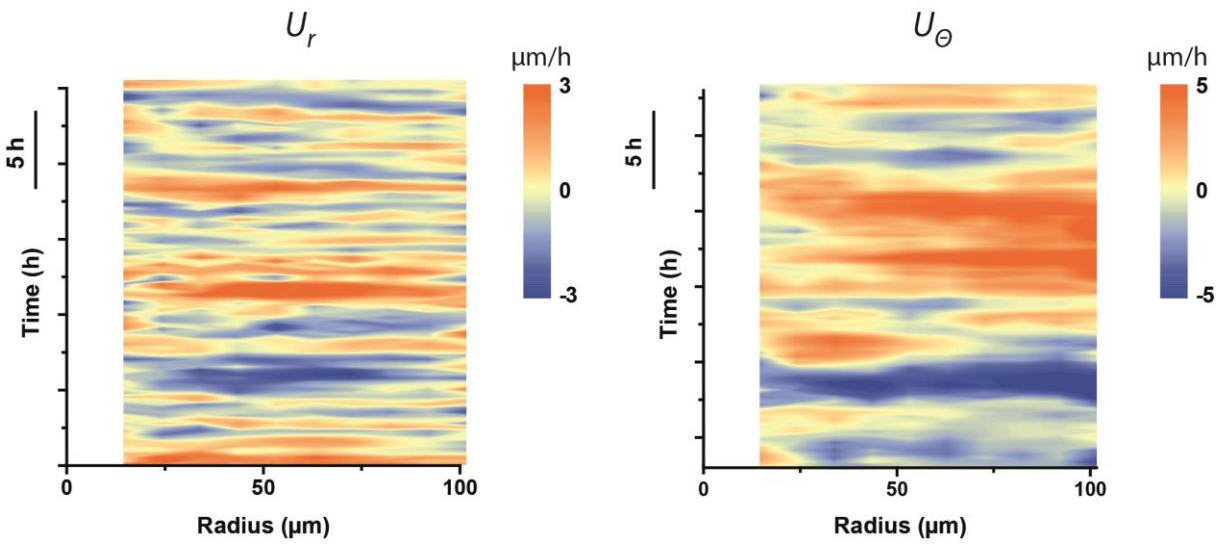

Supplementary Figure 11: The spatio-temporal evolution of the velocity components in the simulations compares well with the experiments. Heatmaps of the two components of the velocity generated by the simulations. They are very similar to the experimental ones (Fig. 2B,C). The origin of the time scale is arbitrary since the number of cells was kept constant in the simulations.

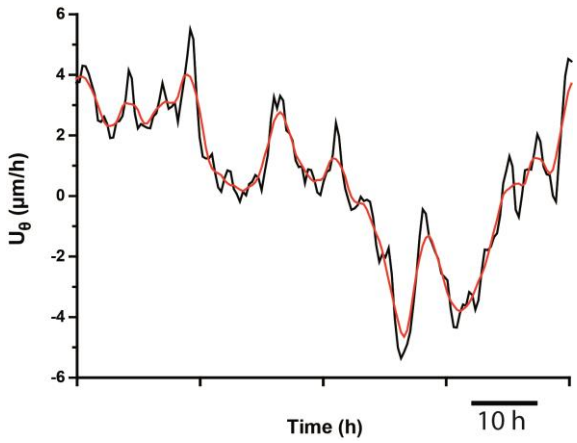

Supplementary Figure 12: Simulations of the time fluctuations of the orthoradial velocity. These simulations were performed in the same conditions as Figure 2F. Note that in those simulations, the density was kept constant and therefore the damping of the oscillations due to cell jamming at high densities is not observed.

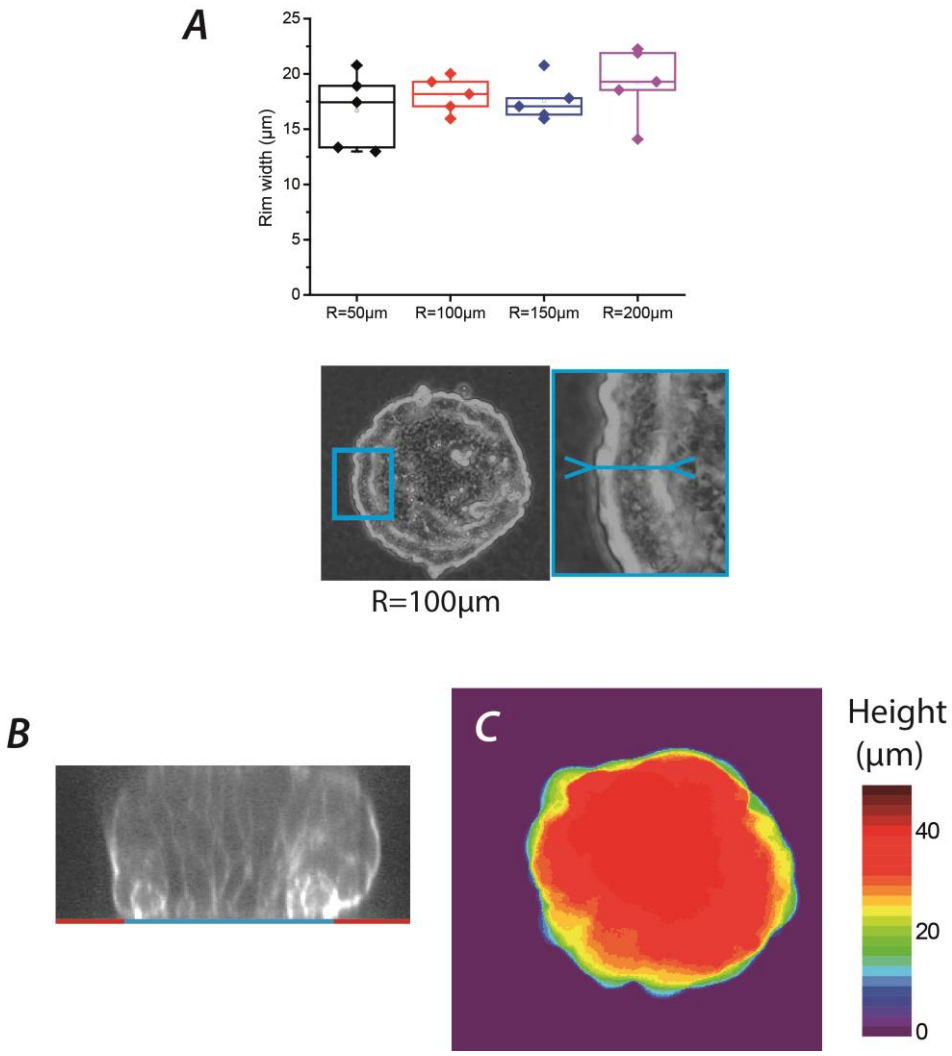

Supplementary Figure 13: The rim is an intrinsic characteristic of the cell population. A. the rim width is independent from the size of the domain. Widths were measured between the outermost edge and the white ring denoting a steep edge in phase contrast (see inset). Differences in the rim width according to domain radius are not significant (2 sample t-test, n=5, 2 experiments). **B. Droplet-like shape of cell aggregates on small domains.** When the radius of the patches is smaller than the typical width of the rim, the whole structure merged into a droplet-like structure. The domain diameter (in blue) is 50 µm. t=150h. 12 replicates. **C.** Color coded 3D reconstructions of the same droplet.

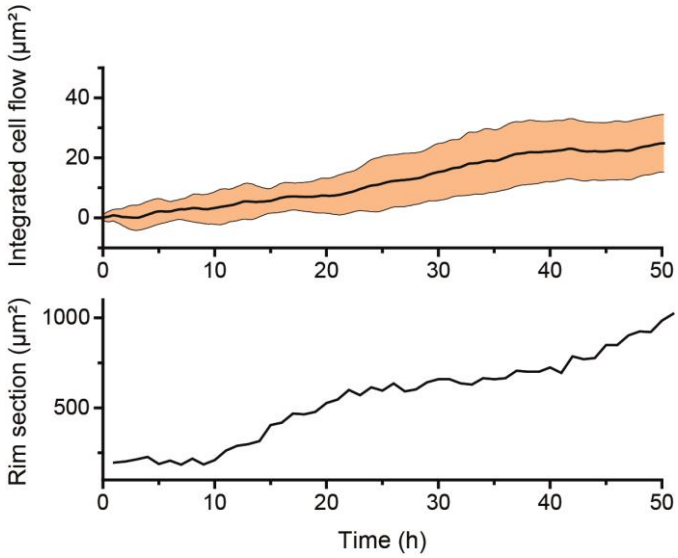

Supplementary Figure 14: Rims do not result from a net centrifugal cell flow. Flow calculated by PIV was multiplied by monolayer thickness (typically e= 5µm) and integrated with time (top panel). The contribution of this centrifugal flow is very small compared to the increase of rim size (bottom panel, note the difference in y-scales between the two panels). The centrifugal radial displacements in the monolayer contribute very little to rim formation and development. R= 50 µm. Representative plot, 15 replicates for domain radii ranging from 50 to 150 µm.

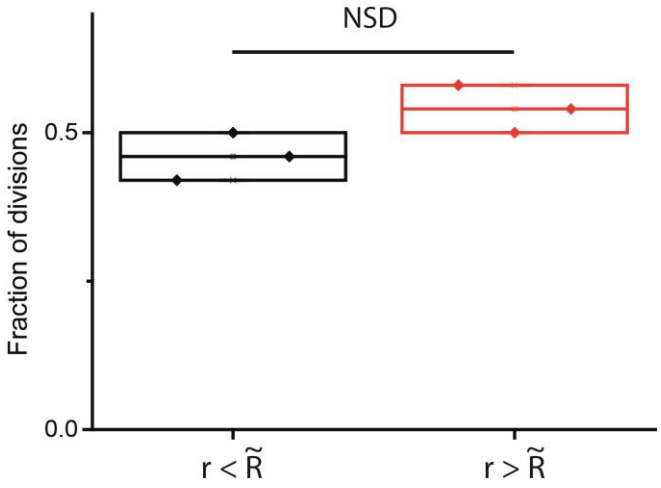

Supplementary Figure 15: Initial uniform proliferation. In the first 25h after confluence, proliferation was homogeneous throughout the domains ($\tilde{R} = R - 50\mu m$). The number of division events has been normalized by the corresponding surface. There was no more divisions for $\tilde{R}$<r<R compared to 0<r< $\tilde{R}$ (t-test, n=3). 2 independent experiments (R=100 µm and R=200 µm).

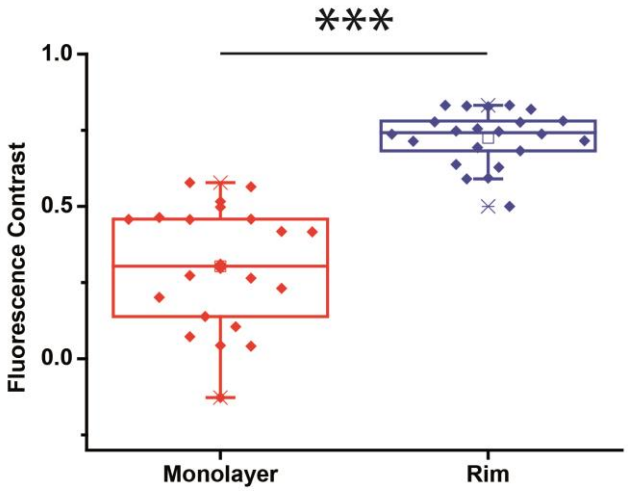

Supplementary Figure 16: Collective dorso-ventral polarity. The rim and the monolayer polarize rapidly after confluence. The polarity at the rim is defined at the pluricellular scale. Ezrin signal inside the rim remained weak (Figure 4D). The polarity contrast defined as the normalized difference between apical and basal fluorescence signals, is significantly larger at the rim compared to the monolayer (n=22 over 3 experiments, $p<<10^{-9}$, 2-sample t test). t=100h.

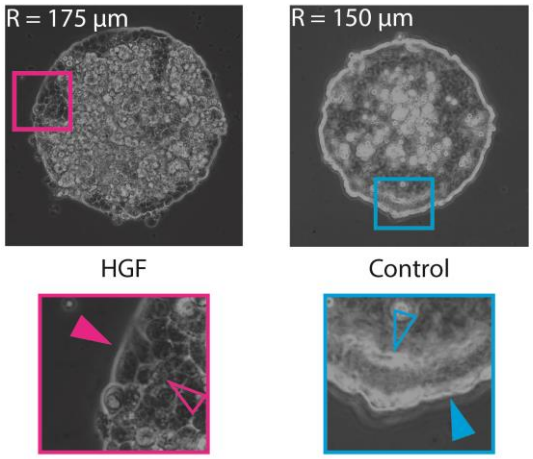

Supplementary Figure 17: Peripheral cells cords are collective structures. HGF destabilizes rims at long times (t=90h) as can be assessed by the absence of the phase contrast ring visible in control situations (empty triangles). The bright outermost halo present in control conditions but absent in HGF conditions is another signature of the rim (full triangles). HGF was added 13h after confluence. Phase contrast images. Rims are systematically present in control conditions and systematically absent in presence of HGF (triangles).

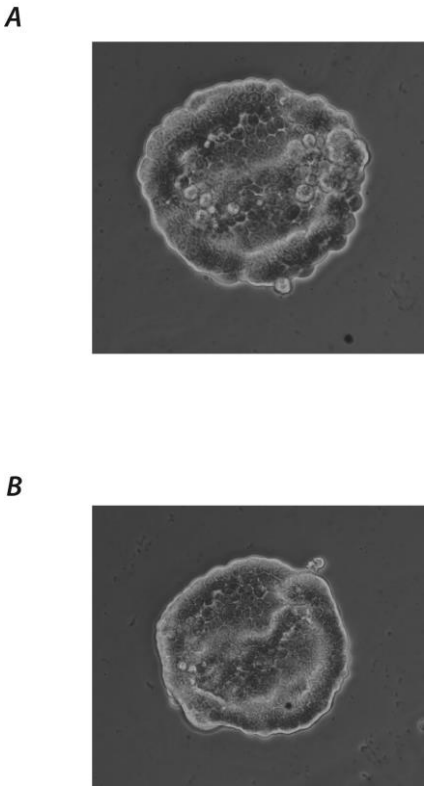

Supplementary Figure 18: .Morphogenesis and maintenance of the rim do not depend on contractility. A. Treatment with Blebbistatin 10h after rim formation did not result in its destabilization, showing that rim maintenance does not depend on contractility. R= 75 µm ; Observation 10 hrs after myosin inhibition ; 5 replicates. **B.** When the drug was added before rim formation (5 to 15 h after confluence), the rim developed similarly as the control. Therefore, rim morphogenesis does not depend on contractility. R= 100 µm, inhibition 14h after confluence, observation 34h after confluence, 5 replicates.

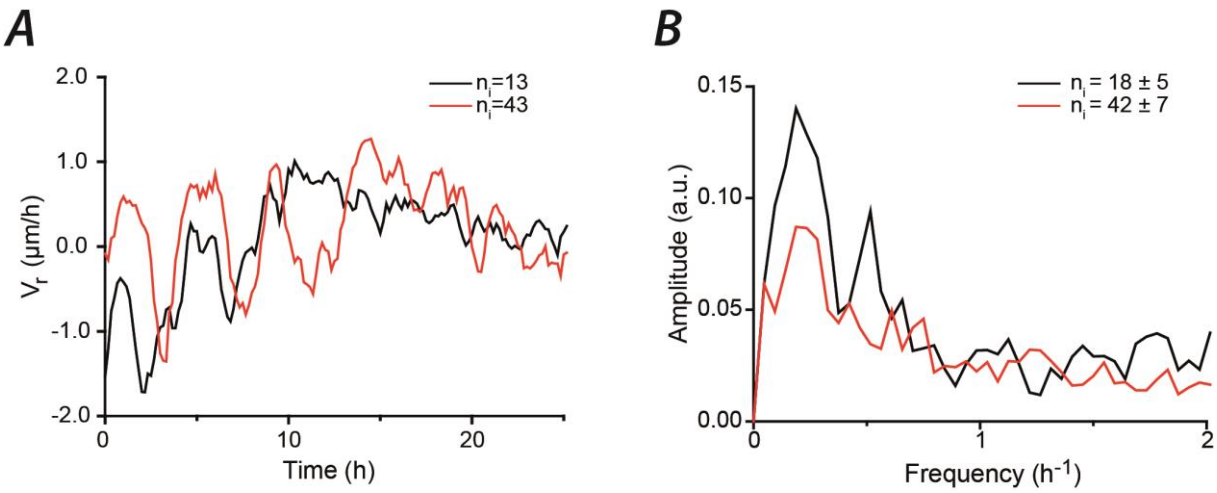

Supplementary Figure 19: The oscillations are independent from the initial number of cells. A) Oscillations of the radial velocity for two different initial seeding densities. R=100µm. n_i is the initial number of cells in the domain. t=0 the time at which the cells reach confluence. Representative plots, 13 replicates. B) FFT spectra obtained for different initial cell densities (n=4 for n_i = 18 ± 5 (SD) ; n=7 for n_i = 42 ± 7 (SD)). Both spectra give the same peak position (resp. 0.22 ± 0.01 h^{-1} and 0.23 ± 0.01 h^{-1} as obtained from gaussian fits as described in the text).